








RESEARCH ARTICLE | AUGUST 30 2023

The effect of axisymmetric confinement on propulsion of a three-sphere microswimmer

Ali Gürbüz ; Andrew Lemus ; Ebru Demir ; On Shun Pak  ; Abdallah Daddi-Moussa-Ider  



Physics of Fluids 35, 081907 (2023)

<https://doi.org/10.1063/5.0163348>



View
Online



Export
Citation

CrossMark

Articles You May Be Interested In

Synthesis of magneto-responsive microswimmers for biomedical applications

AIP Advances (February 2021)

Model microswimmers in channels with varying cross section

J. Chem. Phys. (May 2017)

Dynamical density functional theory for microswimmers

J. Chem. Phys. (January 2016)

The effect of axisymmetric confinement on propulsion of a three-sphere microswimmer

Cite as: Phys. Fluids **35**, 081907 (2023); doi: [10.1063/5.0163348](https://doi.org/10.1063/5.0163348)

Submitted: 16 June 2023 · Accepted: 10 August 2023 ·

Published Online: 30 August 2023



View Online



Export Citation



CrossMark

Ali Gürbüz,¹  Andrew Lemus,¹  Ebru Demir,²  On Shun Pak,^{1,3,a)}  and Abdallah Daddi-Moussa-Ider^{4,a)} 

AFFILIATIONS

¹Department of Mechanical Engineering, Santa Clara University, Santa Clara, California 95053, USA

²Department of Mechanical Engineering and Mechanics, Lehigh University, Bethlehem, Pennsylvania 18015, USA

³Department of Applied Mathematics, Santa Clara University, Santa Clara, California, 95053, USA

⁴Max Planck Institute for Dynamics and Self-Organization, 37077 Göttingen, Germany

^{a)} Authors to whom correspondence should be addressed: opak@scu.edu and abdallah.daddi-moussa-ider@ds.mpg.de

ABSTRACT

Swimming at the microscale has recently garnered substantial attention due to the fundamental biological significance of swimming microorganisms and the wide range of biomedical applications for artificial microswimmers. These microswimmers invariably find themselves surrounded by different confining boundaries, which can impact their locomotion in significant and diverse ways. In this work, we employ a widely used three-sphere swimmer model to investigate the effect of confinement on swimming at low Reynolds numbers. We conduct theoretical analysis via the point-particle approximation and numerical simulations based on the finite element method to examine the motion of the swimmer along the centerline in a capillary tube. The axisymmetric configuration reduces the motion to one-dimensional movement, which allows us to quantify how the degree of confinement affects the propulsion speed in a simple manner. Our results show that the confinement does not significantly affect the propulsion speed until the ratio of the radius of the tube to the radius of the sphere is in the range of $\mathcal{O}(1) - \mathcal{O}(10)$, where the swimmer undergoes substantial reduction in its propulsion speed as the radius of the tube decreases. We provide some physical insights into how reduced hydrodynamic interactions between moving spheres under confinement may hinder the propulsion of the three-sphere swimmer. We also remark that the reduced propulsion performance stands in stark contrast to the enhanced helical propulsion observed in a capillary tube, highlighting how the manifestation of confinement effects can vary qualitatively depending on the propulsion mechanisms employed by the swimmers.

© 2023 Author(s). All article content, except where otherwise noted, is licensed under a Creative Commons Attribution (CC BY) license (<http://creativecommons.org/licenses/by/4.0/>). <https://doi.org/10.1063/5.0163348>

I. INTRODUCTION

The study of locomotion in fluids at the microscopic scale has attracted significant attention in recent decades. This growing interest is not only driven by the motivation to better understand the motility of swimming microorganisms^{1–3} but also the potential biomedical applications of artificial microswimmers such as targeted drug delivery and minimally invasive microsurgery.^{4–9} Locomotion of biological and artificial microswimmers occurs at negligibly small Reynolds numbers (Re), where viscous forces largely dominate inertial forces. In the inertialess regime, the ability to self-propel is severely constrained owing to kinematic reversibility. In particular, Purcell's scallop theorem¹⁰ states that in the absence of inertia, deformations exhibiting time-reversal symmetry (e.g., the motion of a single-hinged scallop opening and closing its shell), also known as reciprocal motion, are unable to produce any net self-propulsion. Common macroscopic swimming

strategies such as rigid flapping motion hence become largely ineffective at low Re. Microorganisms such as bacteria and spermatozoa have evolved strategies that utilize biological appendages called flagella with the action of molecular motors to swim in their microscopic world. Extensive studies in the past decades have elucidated the physical principles underlying their motility.^{11–16}

In parallel efforts, researchers have sought simple and effective mechanisms to develop artificial microswimmers.^{17–20} In his pioneering work, Purcell demonstrated how a three-link swimmer,¹⁰ now known as Purcell's swimmer,^{21–25} can generate net translation with kinematically irreversible cyclic motions. This elegant example has inspired the subsequent development of mechanisms that can overcome the fundamental challenge of generating self-propulsion in the inertialess regime. In particular, Najafi and Golestanian²⁶ developed a swimmer consisting of three spheres connected by two extensible rods,

which adjust their lengths in a cyclic manner to ingeniously exploit hydrodynamic interactions between the spheres for self-propulsion. The mechanism has also engendered a variety of variants^{27–37} and their experimental realizations.^{38–41} For its simplicity, the three-sphere swimmer has gained popularity as a useful model for examining different fundamental aspects of locomotion at low Re, including the effect of complex rheology,^{42,43} optimized locomotion,^{34,35} interactions of swimmers,^{43–45} and swimming near walls.^{46–49} The three-sphere model has further been used to investigate the reorientation dynamics of microswimmers with respect to flow gradients (rheotaxis),⁵⁰ finding that payloads can be exploited to enhance their motion against flows. More recently, the model has also been employed to explore the integration with machine learning in realizing smart microswimmers.^{51–55}

Here, we utilize the three-sphere swimmer model to probe the effect of confinement on swimming at low Re. Microswimmers invariably find themselves surrounded by different confining boundaries. Extensive studies have demonstrated how swimming near planar boundaries can impact locomotion in significant and diverse manners.^{46–49,56–68} Microorganisms also encounter more complex confinements than planar boundaries, such as spermatozoa swimming through fallopian tubes, parasites *Trypanosomes* in blood vessels, and bacterial motion in microporous soil environments. For swimming inside a capillary tube, previous studies have shown that whether the confinement enhances or hinders propulsion largely depends on the type of swimmers.^{69–75} For instance, rotating helical flagella, which generate propulsion as a result of drag anisotropy of the slender flagella, display enhanced propulsion speeds inside a capillary tube.⁷³ However, squirmers with the distribution of tangential surface velocities always have reduced propulsion speeds.⁷¹ These results suggest that the difference in the propulsion mechanism of the swimmers plays significant roles in how the confinement impacts propulsion. In this work, we consider another physically different propulsion mechanism, namely, the three-sphere swimmer model, which relies on the hydrodynamic interaction between the spheres for self-propulsion. For simplicity, we focus on the effect of axisymmetric confinement

when the swimmer self-propels along the centerline inside a capillary tube. We use both the point-particle approximation and the finite element method to quantify how the degree of confinement affects the propulsion speed of this widely used swimmer model. We also provide some physical insights into the underlying mechanism by which confinement influences this specific mode of propulsion.

This paper is organized as follows. We formulate the problem in Sec. II by presenting the swimmer model, the geometrical setup, and the methods of analysis. In Sec. III, we first validate our theoretical and numerical results by revisiting the case of an unbounded fluid domain (Sec. III A), before discussing new results for confined swimming (Sec. III B). We conclude this study in Sec. IV with remarks on its limitations and potential directions for future studies.

II. PROBLEM FORMULATION

A. Swimmer model

We consider the motion of a three-sphere microswimmer confined axisymmetrically in a capillary tube of radius R_c . The swimmer was first studied in an unbounded fluid domain by Najafi and Golestanian.²⁶ As illustrated in Fig. 1(a), the swimmer consists of three spheres of the same radius R connected by two extensible rods of negligible hydrodynamic influences. The fully extended length of each arm is given by D and the fully contracted length of each arm is given by $D - \epsilon$, where ϵ denotes the amount of contraction or extension in each stroke (referred to as the contraction length hereafter). In the main text, we follow Najafi and Golestanian²⁶ to consider a constant relative speed W in the change of the arm length in the four strokes illustrated in Fig. 1(b): in stroke I, the swimmer contracts its left arm of an initial length D by an amount ϵ , keeping the length of the right arm at D . In stroke II, the swimmer contracts its right arm by an amount ϵ , keeping the length of the left arm at $D - \epsilon$. In stroke III, the swimmer extends its left arm to reach the fully extended length D , with the length of the right arm fixed at $D - \epsilon$. Finally, in stroke IV, the swimmer extends its right arm to return to its original configuration with both arms fully extended with length D , completing a full swimming cycle. The net displacement generated by such a cycle is

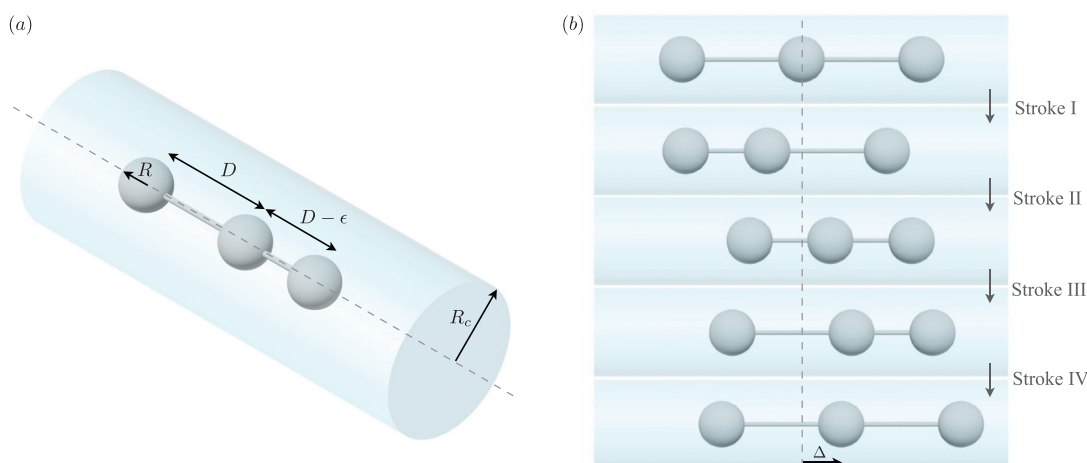


FIG. 1. Schematic of the problem setup and notations. (a) A swimmer consisting of three spheres of equal radii R connected by two extensible rods is confined axisymmetrically in a capillary tube of radius R_c . The rods have a fully extended length of D and a fully contracted length of $D - \epsilon$, where ϵ denotes the amount of contraction. (b) The swimmer undergoes a four-stroke cycle designed by Najafi and Golestanian²⁶ to produce a net displacement, Δ .

denoted by Δ . In addition to these original strokes considered by Najafi and Golestanian,²⁶ harmonic variations of the length of the two rods have been analyzed in subsequent works.⁷⁶ We conduct the same analyses for the case of harmonic deformations of the rods in the Appendix to assess the generality of our findings.

B. Theoretical analysis: point-particle approximation

The motion of an incompressible flow in a Newtonian fluid at low Re is governed by the Stokes equation

$$\begin{aligned} \mu \nabla^2 \mathbf{u} &= \nabla p, \\ \nabla \cdot \mathbf{u} &= 0, \end{aligned} \tag{1}$$

where μ is the dynamic viscosity, and \mathbf{u} and p are, respectively, the fluid velocity and pressure fields. We denote the velocity of the i -th sphere as \mathbf{V}_i and the force and torque acting on them as \mathbf{F}_i and \mathbf{T}_i , respectively. No-slip boundary conditions are applied on the spheres and the confining tube, i.e., $\mathbf{u}_{\text{on the } i\text{-th sphere}} = \mathbf{V}_i$ and $\mathbf{u}_{\text{on the confining tube}} = \mathbf{0}$. Without external forces and external torques, the system should be force-free

$$\sum_{i=1}^3 \mathbf{F}_i = \mathbf{0} \tag{3}$$

and torque-free

$$\sum_{i=1}^3 \mathbf{T}_i = \mathbf{0}. \tag{4}$$

As a remark, the torque-free condition is identically satisfied by the symmetry of the problem setup.

We denote by \mathbf{r}_1 the position of the center sphere, which is chosen as a reference for tracking the movement of the swimmer. We denote by \mathbf{r}_2 and \mathbf{r}_3 the positions of the front and rear spheres, respectively. The temporal change in the mutual distances between the spheres is set to perform a nonreversible time sequence. Under the action of the internally generated forces acting between the spheres along the tube axis (z -axis), the lengths of the rod connecting adjacent spheres are set as

$$(\mathbf{r}_2 - \mathbf{r}_1) \cdot \hat{\mathbf{e}}_z = g(t), \quad (\mathbf{r}_1 - \mathbf{r}_3) \cdot \hat{\mathbf{e}}_z = h(t), \tag{5}$$

where $(g, h) = (D, D - Wt)$ for $t \in [0, T/4]$, $(g, h) = (D + \varepsilon - Wt, D - \varepsilon)$ for $t \in [T/4, T/2]$, $(g, h) = (D - \varepsilon, D - 3\varepsilon + Wt)$ for $t \in [T/2, 3T/4]$, $(g, h) = (D - 4\varepsilon + Wt, D)$ for $t \in [3T/4, T]$, and $\hat{\mathbf{e}}_z$ is the unit vector along the z -direction.

At low Re, inertial effects are negligible so that the immersed particles take on the velocity of the surrounding fluid instantaneously. Accordingly, the translational velocities of the three spheres are related to the internal forces exerted on them linearly via

$$\mathbf{V}_i = \frac{d\mathbf{r}_i}{dt} = \sum_{j=1}^3 \boldsymbol{\mu}_{ij} \cdot \mathbf{F}_j \tag{6}$$

for $i = 1, 2$, and 3 , wherein $\boldsymbol{\mu}_{ij}$ stands for the hydrodynamic mobility tensor relating between the translational velocity of sphere i and the force exerted on sphere j . The hydrodynamic mobility incorporates the effect of the many-body fluid-mediated interactions between suspended particles. Here, we confine ourselves for simplicity to the situation in

which only contributions stemming from self ($i=j$) and pair ($i \neq j$) hydrodynamic interactions are accounted for. We will assess the accuracy of our approach with direct comparison with the fully resolved numerical simulations based on the finite element method (Sec. II C).

In the so-called point-particle approximation, in which $R \ll R_c$, the scaled self-mobility function is given to the leading order in R/R_c by Refs. 77 and 78

$$\frac{\mu_{ii}}{\mu_0} = 1 + \delta \frac{R}{R_c}, \tag{7}$$

wherein $\mu_0 = 1/(6\pi\eta R)$ is the bulk mobility, and

$$\delta = -\frac{3}{2\pi} \int_0^\infty \frac{A(s)}{B(s)} ds. \tag{8}$$

Here, we have defined

$$\begin{aligned} A(s) &= 4I_1(s)K_0(s) + s^2(I_0(s)K_1(s) + I_1(s)K_0(s)) \\ &\quad - 2s(I_0(s)K_0(s) + I_1(s)K_1(s)), \end{aligned} \tag{9a}$$

$$B(s) = 2I_0(s)I_1(s) + s(I_1(s)^2 - I_0(s)^2), \tag{9b}$$

with I_ν and K_ν denoting the ν th order modified Bessel functions (also known as the hyperbolic Bessel functions) of the first and second kinds, respectively. A numerical evaluation of the infinite integral in Eq. (8) yields

$$\delta \simeq -2.10444. \tag{10}$$

Analogously, the hydrodynamic pair mobility in the point-particle approximation is given in a scaled form by Refs. 78 and 79

$$\frac{\mu_{ij}}{\mu_0} = \frac{3}{2} \frac{R}{R_c} \left(\frac{1}{\sigma} + \xi_{ij}(\sigma) \right), \tag{11}$$

where

$$\xi_{ij}(\sigma) = -\frac{1}{\pi} \int_0^\infty \frac{A(s)}{B(s)} \cos(\sigma s) ds, \tag{12}$$

wherein $\sigma = |(\mathbf{r}_i - \mathbf{r}_j) \cdot \hat{\mathbf{e}}_z|/R_c$. Clearly, $\mu_{ij} = \mu_{ji}$, as required by symmetry. In particular, $\delta/\xi(0) = 3/2$.

It is worth noting that the pair mobility can likewise be expressed in terms of the converging infinite series of the form⁸⁰

$$\frac{\mu_{ij}}{\mu_0} = \frac{3}{4} \sum_{n=1}^\infty \varphi_n e^{-\alpha_n \sigma}, \tag{13}$$

where

$$\varphi_n = a_n \cos(\beta_n \sigma) + b_n \sin(\beta_n \sigma). \tag{14}$$

Here, $u_n := \alpha_n + i\beta_n$ are the complex roots of the equation

$$u_n (J_0^2(u_n) + J_1^2(u_n)) = 2J_0(u_n)J_1(u_n) = 0. \tag{15}$$

In addition,

$$\begin{aligned} a_n + ib_n &= 2(\pi(2J_1(u_n)Y_0(u_n) - u_n(J_0(u_n)Y_0(u_n) \\ &\quad + J_1(u_n)Y_1(u_n))) - u_n)/J_1^2(u_n), \end{aligned} \tag{16}$$

where J_ν and Y_ν stand for the ν th order Bessel functions of the first and second kinds, respectively. Accordingly, the pair mobility function

displays a sharp exponential decay as the distance between particles becomes larger. In the limit $\sigma \gg 1$, the series in Eq. (13) can be truncated to the first term to yield

$$\frac{\mu_{ij}}{\mu_0} \simeq \frac{3}{4} (a_1 \cos(\beta_1 \sigma) + b_1 \sin(\beta_1 \sigma)) e^{-\alpha_1 \sigma}, \quad (17)$$

with the numerical estimates $\alpha_1 \simeq 4.466\,30$, $\beta_1 \simeq 1.467\,47$, $a_1 \simeq -0.036\,98$, and $b_1 \simeq 13.808\,21$.

Differentiating Eq. (5) with respect to time yields $V_2 = V_1 + \dot{g}$ and $V_3 = V_1 - \dot{h}$, with dots standing for a time derivative and $V_i = \mathbf{V}_i \cdot \hat{\mathbf{e}}_z$ denotes the axial velocity along the centerline of the confining tube. By requiring the force-free condition Eq. (3), we find that the instantaneous axial velocity of the center sphere is obtained as

$$V_1 = \frac{\dot{h}(\mu_{ii} - \mu_{12})M_+ - \dot{g}(\mu_{ii} - \mu_{13})M_-}{3\mu_{ii}^2 - 2\mu_{ii}(\mu_{12} + \mu_{13} + \mu_{23}) - N}, \quad (18)$$

wherein $M_{\pm} = \mu_{ii} \pm \mu_{12} \mp \mu_{13} - \mu_{23}$ and $N = \mu_{12}^2 + (\mu_{13} - \mu_{23})^2 - 2\mu_{12}(\mu_{13} + \mu_{23})$. We have $(\dot{g}, \dot{h}) = (0, -W)$ for $t \in [0, T/4]$, $(\dot{g}, \dot{h}) = (-W, 0)$ for $t \in [T/4, T/2]$, $(\dot{g}, \dot{h}) = (0, W)$ for $t \in [T/2, 3T/4]$, and $(\dot{g}, \dot{h}) = (W, 0)$ for $t \in [3T/4, T]$. We recall that $\mu_{12} = \mu_{ij}(\sigma = g/R_c)$, $\mu_{13} = \mu_{ij}(\sigma = h/R_c)$, and $\mu_{23} = \mu_{ij}(\sigma = (g + h)/R_c)$. We note that self, μ_{ii} , and pair, μ_{ij} , mobilities are given by Eqs. (7) and (11), respectively.

Finally, the mean swimming velocity is obtained by averaging over one full cycle as

$$\bar{V}_1 = \frac{1}{T} \int_0^T V_1(t) dt. \quad (19)$$

Owing to the delicate and peculiar nature of the resulting axial speed stated by Eq. (18), an analytical evaluation of the mean is rather complicated and far from being trivial, even in the simplistic situation without confinement. To be able to make analytical progress, we expand perturbatively the axial velocity in the small parameter R/D . By substituting the expressions of the self- and pair-mobility functions, given by Eqs. (7) and (11), respectively, into Eq. (18), and noting that $N = \mathcal{O}((R/D)^2)$, the instantaneous swimming velocity can readily, upon the Taylor expansion in the small parameter R/D , be cast in the form

$$V_1 = V_1^B + V_1^C + \mathcal{O}\left(\left(\frac{R}{D}\right)^2\right), \quad (20)$$

where V_1^B is the instantaneous velocity in the absence of confinement, given by

$$V_1^B = \dot{g}((R - 2g)h^2 - 2(R + h)g^2) + \dot{h}((2h - R)g^2 + 2(R + g)h^2) / 6gh(g + h). \quad (21)$$

Moreover, V_1^C is the confinement-related contribution to the instantaneous velocity, given by

$$V_1^C = \frac{R}{6R_c} (\dot{g} \Xi_1 - \dot{h} \Xi_2), \quad (22)$$

wherein $\Xi_1 = \zeta_{12} - 2\zeta_{13} + \zeta_{23}$ and $\Xi_2 = \zeta_{13} - 2\zeta_{12} + \zeta_{23}$.

We find that the bulk-related contribution to the average speed is obtained as

$$\bar{V}_1^B = \frac{R}{3T} \left(\frac{2\varepsilon^2}{D(D - \varepsilon)} + \ln \left(\frac{4D(D - \varepsilon)}{(2D - \varepsilon)^2} \right) \right). \quad (23)$$

In particular, for $\varepsilon \ll D$, we get

$$\bar{V}_1^B = \frac{7R}{12T} \left(\left(\frac{\varepsilon}{D}\right)^2 + \left(\frac{\varepsilon}{D}\right)^3 \right) + \mathcal{O}\left(\left(\frac{\varepsilon}{D}\right)^4\right). \quad (24)$$

The contribution to the averaged speed due to confinement can be approximated in the limit $R \ll D$ as

$$\bar{V}_1^C = \frac{R}{3\pi T} \int_0^\infty \frac{A(s)}{B(s)} \left(\frac{2\varepsilon}{R_c} \psi_1(s) - \frac{\psi_2(s)}{s} \right) ds, \quad (25)$$

where

$$\psi_1(s) = \cos\left(\frac{D}{R_c} s\right) - \cos\left(\frac{D - \varepsilon}{R_c} s\right),$$

$$\psi_2(s) = \sin\left(\frac{2D}{R_c} s\right) - 2 \sin\left(\frac{2D - \varepsilon}{R_c} s\right) + \sin\left(\frac{2(D - \varepsilon)}{R_c} s\right).$$

Here, we have swapped the order of integration with respect to s and t . It is worth highlighting that Eq. (25), which provides the confinement-related contribution to the averaged swimming speed, remains valid across the entire range of values for D and R_c . The only assumption made to derive the approximate expressions for the swimming speed is that R is significantly smaller than D . Since Eq. (25) involves infinite integrals over the scaled wavenumber s , the corresponding analytical expressions cannot be obtained in the limit $\varepsilon \ll D$, unlike the case for the bulk-related contribution given by Eq. (24).

C. Finite element method

We also perform fully coupled numerical simulations of the momentum Eq. (1) and continuity Eq. (2) equations using the finite element method (FEM) implemented in the COMSOL Multiphysics environment. We compare these numerical simulation results, which capture the full sphere-sphere and sphere-confinement hydrodynamic interactions, with predictions based on the point-particle approximation in Sec. II B. The axisymmetry of the problem setup reduces the computational complexity of the problem from three-dimensional to two-dimensional. Since Stokes flows have a slow spatial decay, in order to minimize any hydrodynamic influence from the ends, we consider the cylindrical computational domain of radius R_c and a long axial length of approximately $2000R$ ($1000R$ in each direction away from the outer spheres). The domain is discretized by about 20 000–35 000 P3–P2 (third-order for fluid velocity and second-order for pressure) triangular mesh elements, with the local mesh refinement in the proximity of the three spheres. The degree of freedom is of the order of $(0.5-1) \times 10^6$, depending on the radius of the confining tube. We use the Multifrontal Massively Parallel Sparse (MUMPS) direct solver for all simulations.

Due to the time independence of Stokes flows, the motion of the swimmer is completely determined by its instantaneous movement and geometrical configuration. To simulate the swimming motion over a full cycle, the movement of the swimmer is broken down into separate, stationary simulations for different time instants in

individual strokes. At each instant, the velocities of the spheres are determined by the relative motion of the three spheres plus an unknown swimming speed in the axial direction on all spheres. These prescribed velocities on the spheres are implemented as boundary conditions on the spheres. To determine the unknown swimming speed, the force-free condition Eq. (3) is implemented as a global equation, which is solved together with the momentum and continuity equations to obtain the swimming speed, velocity field, and pressure field simultaneously at each time instant in the swimming cycle. We then perform numerical integration of the swimming speed over a full cycle to obtain the net displacement of the swimmer per cycle, Δ .

III. RESULTS AND DISCUSSION

In Secs. III, we first cross-validate the point-particle approximation and numerical simulations based on the finite element method by considering the motion of a three-sphere swimmer in an unbounded fluid domain in Sec. III A. We then characterize in Sec. III B the effect of axisymmetric confinement on the propulsion performance of the three-sphere swimmer for different levels of confinement and properties of the swimmer.

A. Swimming in an unbounded fluid

For validation, we consider the motion of the three-sphere swimmer in an unbounded fluid domain. In the particle-particle approximation (Sec. II B), the bulk-related contribution to the average speed \bar{V}_1^B is given by Eq. (23), which can be multiplied by the period T to obtain the net displacement of the swimmer per cycle, Δ , shown in Fig. 2 (black solid line). When $\epsilon \ll D$, the net displacement is calculated from Eq. (24) as

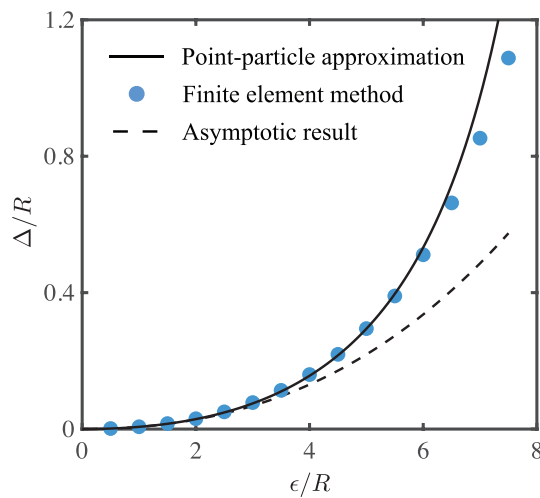


FIG. 2. The scaled net displacement of the swimmer per cycle, Δ/R , in an unbounded fluid as a function of the scaled contraction length of the swimmer, ϵ/R . The black solid line represents results based on the point-particle approximation, $\Delta = \bar{V}_1^B T$, where \bar{V}_1^B is given by Eq. (23), whereas the black dashed line corresponds to the asymptotic results given by Eq. (24) (or Eq. 26) in the limit $\epsilon \ll D$. The blue circles are simulation results based on the finite element method with a large radius of confinement $R_c/R = 1000$ to simulate an unbounded fluid domain. Here, $D/R = 10$.

$$\Delta \sim \frac{7R}{12} \left(\left(\frac{\epsilon}{D} \right)^2 + \left(\frac{\epsilon}{D} \right)^3 \right), \quad (26)$$

which is represented by the black-dashed line in Fig. 2. We remark that the asymptotic result given in Eq. (26) is consistent with that given by Earl *et al.*,²⁸ which rectified the result presented in Najafi and Golestanian.²⁶ The asymptotic result in Eq. (26) reveals that the net displacement of the swimmer per cycle scales quadratically with the contraction length of the swimmer, $\Delta = \mathcal{O}(\epsilon^2)$, in the regime of $\epsilon/D \ll 1$.

To compare with the above theoretical results, in the FEM simulations, we use an exceedingly large radius of confinement ($R_c/R = 1000$) to simulate the swimming motion in an unbounded fluid domain. The FEM results are represented by blue circles in Fig. 2. The comparison between theoretical and numerical results shows that the point-particle approximation captures quantitatively the propulsion behaviors for small to moderate contraction lengths of the swimmer, where the spheres are sufficiently distanced from each other throughout the swimming cycle. For larger contraction lengths, the spheres come closer to each other during contraction, leading to more significant hydrodynamic interactions between the spheres. Consequently, the point-particle approximation starts to deviate from the FEM results, over-estimating the net displacement of the swimmer.^{28,54} Despite these deviations, the point-particle approximation continues to capture the qualitative trend of the propulsion behavior.

B. Swimming under axisymmetric confinement

In Fig. 3, we probe the effect of axisymmetric confinement by examining the net displacement of the three-sphere swimmer along the centerline of a capillary tube. Here, we keep the contraction length

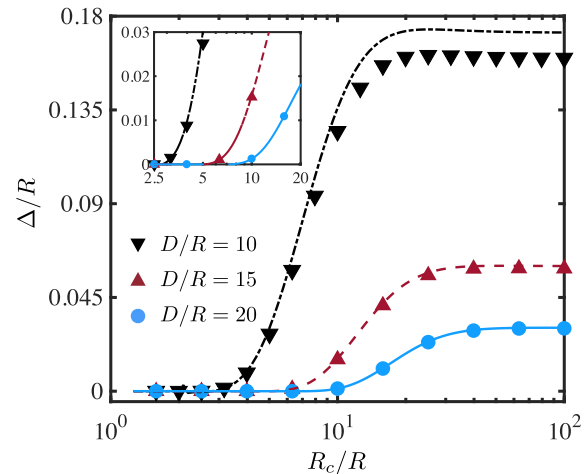


FIG. 3. The scaled net displacement of the swimmer per cycle, Δ/R , as a function of the scaled capillary tube radius, R_c/R , for different values of scaled rod lengths, D/R . Here, $\epsilon/R = 4$. The symbols represent numerical results from FEM simulations (see legends); the lines with the same colors represent the corresponding predictions from the point-particle approximation by integrating the instantaneous velocity given by Eq. (18) over one full cycle. Inset: a magnified view of the relatively small scaled net displacements.

constant ($\epsilon/R = 4$) and only vary the radius of the tube, R_c . For a given fully extended arm length D , the effect of confinement becomes significant when R_c/R is of $\mathcal{O}(1) - \mathcal{O}(10)$: in this regime, the results reveal that a tighter confinement (decreasing R_c) substantially reduces the net displacement of the swimmer. We note that this trend is in stark contrast with the helical propulsion in a capillary tube,⁷³ where the confinement largely enhances propulsion, illustrating how confinement can have qualitatively distinct effects on swimming depending on the underlying propulsion mechanisms. Results from the FEM simulations (symbols) and point-particle approximation (lines) agree well when the spheres are separated by large arm lengths (e.g., $D/R = 15, 20$), when the sphere–sphere and sphere–confinement hydrodynamic interactions are expected to be weaker. For $D/R = 10$, the point-particle approximation still properly captures the qualitative feature of the confined swimming motion when the spheres are in closer proximity, where the near-field effects become more pronounced.

Next, we probe how the net displacement of the swimmer varies with its contraction length when swimming in a capillary tube (Fig. 4). While the net displacement of the swimmer grows with the contraction length in general, it occurs at different rates depending on the degree of confinement (i.e., the value of R_c/R). In an unbounded fluid, the net displacement grows quadratically with the contraction length, $\Delta/R \sim 7\epsilon^2/(12D)$, as given by Eq. (26). In Fig. 4 inset, we consider a log–log plot of the results to better visualize the scaling. For a relatively loose confinement $R_c/R = 10$ (downside black triangles and black dot-dash line), the log–log plot shows an approximately quadratic scaling between the net displacement and the contraction length, similar to the case in an unbounded fluid. However, as the environment becomes more confined ($R_c/R = 2.5$ and 5), results from both point-particle approximation (red dashed line and blue solid line) and FEM

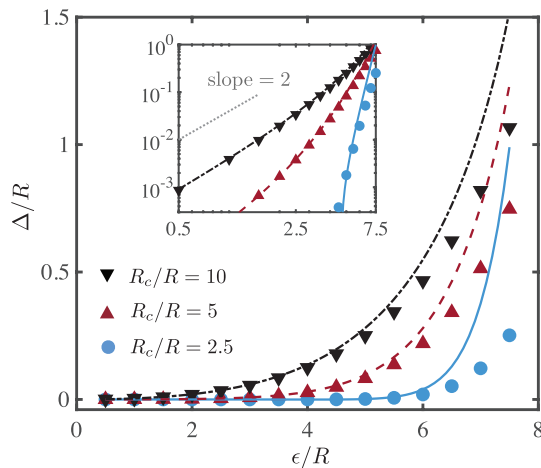


FIG. 4. The scaled net displacement of the swimmer per cycle, Δ/R , as a function of the scaled contraction length of the swimmer, ϵ/R , for different values of the scaled capillary tube radius, R_c/R . Here, $D/R = 10$. The symbols represent numerical results from FEM simulations (see legends); the lines with the same colors represent the corresponding predictions from the point-particle approximation by integrating the instantaneous velocity given by Eq. (18) over one full cycle. The inset displays a log–log plot of the results, where a dotted gray line of slope 2 is added to aid visualization.

(red upside triangles and blue circles) indicate slopes increasingly greater than two in the inset. These results illustrate that the scaling goes beyond second-order in confined swimming; the three-sphere mechanism becomes increasingly ineffective in generating a net displacement under tighter confinement.

To develop a more physical understanding of the above results, we revisit the symmetry arguments by Najafi and Golestanian²⁶ that showed how the four strokes in the cycle are related. These arguments remain valid for the swimmer under axisymmetric confinement considered in this work: stroke III is related to stroke II upon a left–right reflection and a time-reversal transformations, whereas stroke IV is related to stroke I with the same transformations. Consequently, the net displacement of the swimmer after executing a full cycle is simply reduced to (two times) the difference in the net displacement of the center sphere generated by strokes I and II. Stroke I generates a net displacement to the left, while stroke II generates a net displacement to the right. It is crucial to note that these net displacements differ in their magnitudes because the force acting on the spheres when they are far apart (in stroke I) is different from when they are in closer proximity (in stroke II) due to interactions between the spheres via their surrounding flows. The hydrodynamic interactions lead to only partial cancellation of the displacements generated by strokes I and II, giving rise to the net displacement of the swimmer after a cycle. When the hydrodynamic interaction is neglected, the two strokes would generate displacements with equal magnitudes in opposite directions, canceling each other and yielding a zero net propulsion.

Based on the above understanding of the propulsion mechanism, we attribute the reduced net displacement of the confined swimmer to weakened hydrodynamic interactions among the spheres under confinement as follows. It was shown that the flow due to a Stokeslet decays exponentially in a capillary tube due to the confinement,⁸¹ as opposed to decaying as the inverse of the distance in an unbounded fluid. The flow around the moving spheres of the swimmer in a capillary tube is therefore expected to decay more rapidly in space. To visualize this effect, we plot in Fig. 5 the flow field surrounding the swimmer at different time instants in a swimming cycle with different levels of confinement. As the radius of the confining tube decreases from $R_c/R = 10$ in panel (a) to $R_c/R = 2.5$ in panel (c), the magnitude of the flow around individual spheres can be observed to decay more rapidly away from the spheres. These faster spatial decays of the flow velocity weaken the hydrodynamic interaction between the spheres, thereby reducing the hydrodynamic difference between the case when the spheres are more far apart in stroke I and the case when they are in closer proximity in stroke II. The reduced hydrodynamic difference between the two strokes therefore generates displacements with more similar magnitudes, leading to the reduced net displacements of the swimmer in a capillary tube as observed in Fig. 3.

IV. CONCLUDING REMARKS

In this work, we examine the propulsion of a three-sphere swimmer along the centerline of a capillary tube at low Re . We combine the theoretical analysis via the point-particle approximation and simulations based on the finite element method to uncover how the propulsion speed varies with the radius of the confining tube as well as the geometric and kinematic properties of the swimmer. The results show

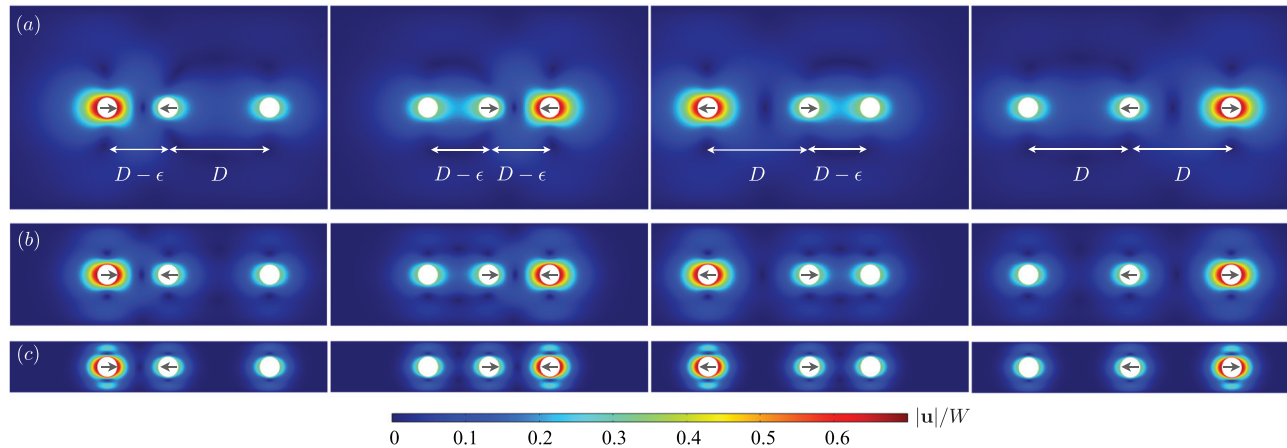


FIG. 5. The scaled flow speed distribution, $|\mathbf{u}|/W$, around the swimmer at the end of individual strokes I–IV (from left to right panels) illustrated in Fig. 1 for different values of the scaled capillary tube radius: (a) $R_c/R = 10$, (b) $R_c/R = 5$, and (c) $R_c/R = 2.5$. The black arrows indicate the relative motion (contraction or extension) of the pair of spheres in different strokes. Here, $D/R = 10$ and $\epsilon/R = 4$.

that the presence of confinement does not significantly affect the propulsion speed until the scaled radius of the confining tube is in the range of $R_c/R = \mathcal{O}(1) - \mathcal{O}(10)$, where the swimmer exhibits sharp decays in propulsion speed as the radius of the tube decreases. The presence of confinement also leads to a higher-order scaling between the net displacement and the contraction length of the swimmer, reducing the effectiveness of this propulsion mechanism. We contrast the reduced propulsion speed observed here with the enhanced helical propulsion inside a capillary tube reported earlier,⁷³ highlighting how the effect of confinement can manifest in qualitatively different manners depending on the swimmer's propulsion mechanism. While helical propulsion is based on the drag anisotropy of slender bodies, the three-sphere swimmer here relies on the sphere–sphere hydrodynamic interactions—a physically different mechanism—to self-propel. The reduced propulsion performance observed here is attributed to the more rapid spatial decays of the flow velocity of moving bodies in a tube, which reduces the hydrodynamic interaction between the spheres and thereby the net displacement of the swimmer.

Based on the above physical understanding of the results, we hypothesize that the propulsion of a three-sphere swimmer in porous media may also be hindered due to the screening of hydrodynamic interactions by networks of obstacles, in contrast to enhanced propulsion predicted for different types of swimmers in heterogeneous viscous environments.^{82–88} An investigation is under way to evaluate this hypothesis and will be reported in a future work. Furthermore, we considered the effect due to rigid confinement in this work, while the fluid–structure interaction between the swimmer and elastic confinements can have profound impacts on the swimming performance.^{72,89,90} It would be worthwhile to consider the case of an elastic tube and systematically examine the interplay between shear and bending deformation modes in prescribing the hydrodynamics of the swimmer under elastic confinement. Finally, we focus on the effect of axisymmetric confinement here to preserve the one-dimensional nature of the motion, which allows us to measure how the degree of confinement affects the propulsion speed in a simple manner. Lifting this restriction to examine more general motion of a three-sphere

swimmer in a capillary tube could lead to more complex and interesting swimming dynamics in future studies.

ACKNOWLEDGMENTS

O.S.P. acknowledges funding support by the National Science Foundation (Grant Numbers 1830859 and 1931292). A.D.-M.-I. acknowledges support from the Max Planck Center Twente for Complex Fluid Dynamics, the Max Planck School Matter to Life, and the MaxSynBio Consortium, which are jointly funded by the Federal Ministry of Education and Research (BMBF) of Germany and the Max Planck Society. The authors are also grateful for the computational resources from the WAVE computing facility (enabled by the E. L. Wiegand Foundation) at Santa Clara University.

AUTHOR DECLARATIONS

Conflict of Interest

The authors have no conflicts to disclose.

Author Contributions

Ali Gurbuz: investigation (equal); software (equal); writing—original draft (equal); and writing—review and editing (equal). **Andrew Lemus:** investigation (equal); software (equal); writing—original draft (equal); and writing—review and editing (equal). **Ebru Demir:** software (equal); writing—review and editing (equal). **On Shun Pak:** conceptualization (equal); funding acquisition (equal); investigation (equal); resources (equal); supervision (equal); writing—original draft (equal); and writing—review and editing (equal). **Abdallah Daddi-Moussa-Ider:** conceptualization (equal); investigation (equal); methodology (equal); supervision (equal); writing—original draft (equal); and writing—review and editing (equal).

DATA AVAILABILITY

The data that support the findings of this study are available from the corresponding author upon reasonable request.

APPENDIX: A CONFINED THREE-SPHERE SWIMMER WITH HARMONIC OSCILLATIONS OF THE ROD LENGTHS

We follow Najafi and Golestanian²⁶ in the main text in considering a constant relative speed W in the change of arm length. In this appendix, we also consider harmonic deformations of the arms⁷⁶ to establish some generality of the conclusion. Specifically, we prescribe the following variations, respectively, for the length of the front and rear rods:

$$g(t) = D - \frac{\varepsilon}{2} + \frac{\varepsilon}{2} \cos(\omega t), \tag{A1}$$

$$h(t) = D - \frac{\varepsilon}{2} + \frac{\varepsilon}{2} \cos(\omega t + \phi). \tag{A2}$$

The two rods have an equilibrium length of $D - \varepsilon/2$ with sinusoidal oscillations of amplitude $\varepsilon/2$, angular frequency ω , and a phase mismatch ϕ . Here, we set $\omega = \pi W/\varepsilon$, so that the period of oscillation is given by $T = 2\varepsilon/W$. As a remark, when $\phi = 0$, the swimmer generates a zero net propulsion by symmetry; when $\phi = \pi$, the overall deformation of the swimmer becomes a reciprocal motion, which also leads to a zero net propulsion as dictated by the scallop theorem. Here, we present results for the specific case of $\phi = \pi/2$, which was shown to generate the maximum amount of net displacement of the swimmer in an unbounded fluid.⁷⁶ As shown in Figs. 6 and 7, a confined swimmer with harmonic variations of its arm lengths exhibits qualitatively the same behaviors, compared with the case of a constant rate of change of the arm lengths examined in the main text (Figs. 3 and 4).

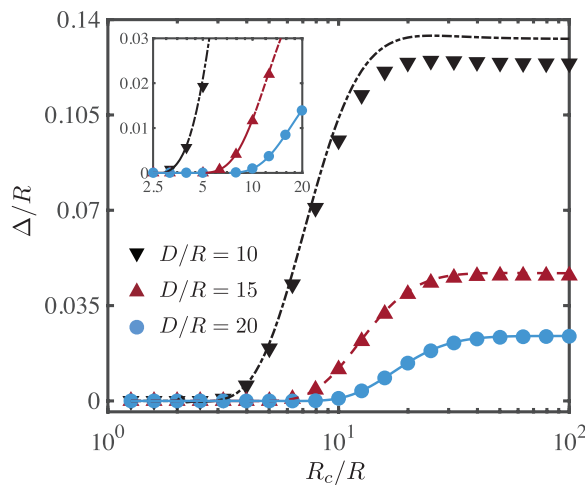


FIG. 6. The scaled net displacement of the swimmer per cycle, Δ/R , as a function of the scaled capillary tube radius, R_c/R , for different values of scaled rod lengths, D/R , for the case of harmonic deformations prescribed by Eqs. (A1) and (A2). Here, $\varepsilon/R = 4$. The symbols represent numerical results from FEM simulations (see legends); the lines with the same colors represent the corresponding predictions from the point-particle approximation by integrating the instantaneous velocity given by Eq. (18) over one full cycle. Inset: a magnified view of the relatively small scaled net displacements.

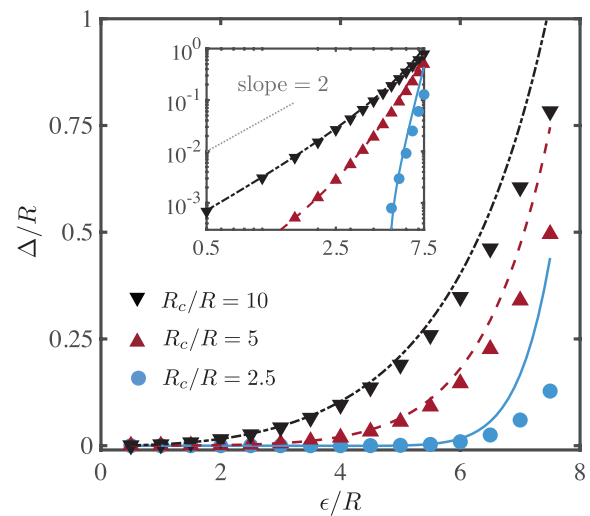


FIG. 7. The scaled net displacement of the swimmer per cycle, Δ/R , as a function of the scaled contraction length of the swimmer, ε/R , for different values of the scaled capillary tube radius, R_c/R , for the case of harmonic deformations prescribed by Eqs. (A1) and (A2). Here, $D/R = 10$. The symbols represent numerical results from FEM simulations (see legends); the lines with the same colors represent the corresponding predictions from the point-particle approximation by integrating the instantaneous velocity given by Eq. (18) over one full cycle. The inset displays a log–log plot of the results, where a dotted gray line of slope 2 is added to aid visualization.

REFERENCES

- ¹C. Brennen and H. Winet, “Fluid mechanics of propulsion by cilia and flagella,” *Annu. Rev. Fluid Mech.* **9**, 339–398 (1977).
- ²D. Bray, *Cell Movements* (Garland, New York, 2001).
- ³E. Lauga, *The Fluid Dynamics of Cell Motility* (Cambridge University Press, Cambridge, UK, 2020), Vol. 62.
- ⁴B. J. Nelson, I. K. Kaliakatsos, and J. J. Abbott, “Microrobots for minimally invasive medicine,” *Annu. Rev. Biomed. Eng.* **12**, 55–85 (2010).
- ⁵M. Sitti, H. Ceylan, W. Hu, J. Giltinan, M. Turan, S. Yim, and E. Diller, “Biomedical applications of untethered mobile milli/microrobots,” *Proc. IEEE* **103**, 205–224 (2015).
- ⁶J. Li, B. Esteban-Fernández de Ávila, W. Gao, L. Zhang, and J. Wang, “Micro/nanorobots for biomedicine: Delivery, surgery, sensing, and detoxification,” *Sci. Rob.* **2**, eaam6431 (2017).
- ⁷W. Hu, G. Z. Lum, M. Mastrangeli, and M. Sitti, “Small-scale soft-bodied robot with multimodal locomotion,” *Nature* **554**, 81–85 (2018).
- ⁸S. Palagi and P. Fischer, “Bioinspired microrobots,” *Nat. Rev. Mater.* **3**, 113–124 (2018).
- ⁹A. C. Tsang, E. Demir, Y. Ding, and O. S. Pak, “Roads to smart artificial micro-swimmers,” *Adv. Intell. Syst.* **2**, 1900137 (2020).
- ¹⁰E. M. Purcell, “Life at low Reynolds number,” *Am. J. Phys.* **45**, 3–11 (1977).
- ¹¹L. J. Fauci and R. Dillon, “Biofluidmechanics of reproduction,” *Annu. Rev. Fluid Mech.* **38**, 371–394 (2006).
- ¹²E. Lauga and T. R. Powers, “The hydrodynamics of swimming microorganisms,” *Rep. Prog. Phys.* **72**, 096601 (2009).
- ¹³J. M. Yeomans, D. O. Pushkin, and H. Shum, “An introduction to the hydrodynamics of swimming microorganisms,” *Eur. Phys. J.* **223**, 1771–1785 (2014).
- ¹⁴C. Bechinger, R. Di Leonardo, H. Löwen, C. Reichhardt, G. Volpe, and G. Volpe, “Active particles in complex and crowded environments,” *Rev. Mod. Phys.* **88**, 045006 (2016).
- ¹⁵E. Lauga, “Bacterial hydrodynamics,” *Annu. Rev. Fluid Mech.* **48**, 105–130 (2016).
- ¹⁶K. Wan, “The beat of isolated cilia,” *Nat. Phys.* **18**, 234–235 (2022).

- ¹⁷J. J. Abbott, K. E. Peyer, M. C. Lagomarsino, L. Zhang, L. Dong, I. K. Kaliakatsos, and B. J. Nelson, "How should microrobots swim?," *Int. J. Rob. Res.* **28**, 1434–1447 (2009).
- ¹⁸S. J. Ebbens and J. R. Howse, "In pursuit of propulsion at the nanoscale," *Soft Matter* **6**, 726–738 (2010).
- ¹⁹E. Lauga, "Life around the scallop theorem," *Soft Matter* **7**, 3060–3065 (2011).
- ²⁰P. Sharan, A. Daddi-Moussa-Ider, J. Agudo-Canalejo, R. Golestanian, and J. Simmchen, "Pair interaction between two catalytically active colloids," *Small* (in press).
- ²¹L. E. Becker, S. A. Koehler, and H. A. Stone, "On self-propulsion of micro-machines at low Reynolds number: Purcell's three-link swimmer," *J. Fluid Mech.* **490**, 15–35 (2003).
- ²²D. Tam and A. E. Hosoi, "Optimal stroke patterns for Purcell's three-link swimmer," *Phys. Rev. Lett.* **98**, 068105 (2007).
- ²³J. E. Avron and O. Raz, "A geometric theory of swimming: Purcell's swimmer and its symmetrized cousin," *New J. Phys.* **10**, 063016 (2008).
- ²⁴K. Qin, Z. Zou, L. Zhu, and O. S. Pak, "Reinforcement learning of a multi-link swimmer at low Reynolds numbers," *Phys. Fluids* **35**, 032003 (2023).
- ²⁵K. Qin and O. S. Pak, "Purcell's swimmer in a shear-thinning fluid," *Phys. Rev. Fluids* **8**, 033301 (2023).
- ²⁶A. Najafi and R. Golestanian, "Simple swimmer at low Reynolds number: Three linked spheres," *Phys. Rev. E* **69**, 062901 (2004).
- ²⁷J. E. Avron, O. Kenneth, and D. H. Oaknin, "Pushmepullyou: An efficient micro-swimmer," *New J. Phys.* **7**, 234 (2005).
- ²⁸D. J. Earl, C. M. Pooley, J. F. Ryder, I. Bredberg, and J. M. Yeomans, "Modeling microscopic swimmers at low Reynolds number," *J. Chem. Phys.* **126**, 064703 (2007).
- ²⁹R. Golestanian and A. Ajdari, "Stochastic low Reynolds number swimmers," *J. Phys.: Condens. Matter* **21**, 204104 (2009).
- ³⁰F. Alouges, A. DeSimone, and A. Lefebvre, "Optimal strokes for low Reynolds number swimmers: An example," *J. Nonlinear Sci.* **18**, 277–302 (2008).
- ³¹F. Alouges, A. DeSimone, L. Heltai, A. Lefebvre-Lepot, and B. Merlet, "Optimally swimming Stokesian robots," *Discrete Contin. Dyn. Syst., Ser. B* **18**, 1189 (2013).
- ³²A. Montino and A. DeSimone, "Three-sphere low-Reynolds-number swimmer with a passive elastic arm," *Eur. Phys. J. E* **38**, 42 (2015).
- ³³Q. Wang and H. G. Othmer, "Analysis of a model microswimmer with applications to blebbing cells and mini-robots," *J. Math. Biol.* **76**, 1699–1763 (2018).
- ³⁴Q. Wang, "Optimal strokes of low Reynolds number linked-sphere swimmers," *Appl. Sci.* **9**, 4023 (2019).
- ³⁵B. Nasouri, A. Vilfan, and R. Golestanian, "Efficiency limits of the three-sphere swimmer," *Phys. Rev. Fluids* **4**, 073101 (2019).
- ³⁶Y. Liu, Z. Zou, A. C. H. Tsang, O. S. Pak, and Y.-N. Young, "Mechanical rotation at low Reynolds number via reinforcement learning," *Phys. Fluids* **33**, 062007 (2021).
- ³⁷I. Berdakin, V. I. Marconi, and A. J. Banchio, "Boosting micromachine studies with Stokesian dynamics," *Phys. Fluids* **34**, 037102 (2022).
- ³⁸M. Leoni, J. Kotar, B. Bassetti, P. Cicuta, and M. C. Lagomarsino, "A basic swimmer at low Reynolds number," *Soft Matter* **5**, 472–476 (2009).
- ³⁹G. Grosjean, M. Hubert, G. Lagubeau, and N. Vandewalle, "Realization of the Najafi-Golestanian microswimmer," *Phys. Rev. E* **94**, 021101(R) (2016).
- ⁴⁰F. Box, E. Han, C. R. Tipton, and T. Mullin, "On the motion of linked spheres in a Stokes flow," *Exp. Fluids* **58**, 29 (2017).
- ⁴¹O. Silverberg, E. Demir, G. Mishler, B. Hosoume, N. Trivedi, C. Tisch, D. Plascencia, O. S. Pak, and I. E. Araci, "Realization of a push-me-pull-you swimmer at low Reynolds numbers," *Bioinspiration Biomimetics* **15**, 064001 (2020).
- ⁴²M. P. Curtis and E. A. Gaffney, "Three-sphere swimmer in a nonlinear visco-elastic medium," *Phys. Rev. E* **87**, 043006 (2013).
- ⁴³K. Yasuda, Y. Hosaka, and S. Komura, "Generalized three-sphere micro-swimmers," *J. Phys. Soc. Japan* (unpublished).
- ⁴⁴C. M. Pooley, G. P. Alexander, and J. M. Yeomans, "Hydrodynamic interaction between two swimmers at low Reynolds number," *Phys. Rev. Lett.* **99**, 228103 (2007).
- ⁴⁵M. Farzin, K. Ronasi, and A. Najafi, "General aspects of hydrodynamic interactions between three-sphere low-Reynolds-number swimmers," *Phys. Rev. E* **85**, 061914 (2012).
- ⁴⁶R. Zargar, A. Najafi, and M. Miri, "Three-sphere low-Reynolds-number swimmer near a wall," *Phys. Rev. E* **80**, 026308 (2009).
- ⁴⁷A. Najafi, S. S. H. Raad, and R. Yousefi, "Self-propulsion in a low-Reynolds-number fluid confined by two walls of a microchannel," *Phys. Rev. E* **88**, 045001 (2013).
- ⁴⁸A. Daddi-Moussa-Ider, M. Lisicki, A. J. T. M. Mathijssen, C. Hoell, S. Goh, J. Bławdziewicz, A. M. Menzel, and H. Löwen, "State diagram of a three-sphere microswimmer in a channel," *J. Phys.: Condens. Matter* **30**, 254004 (2018).
- ⁴⁹A. Daddi-Moussa-Ider, M. Lisicki, C. Hoell, and H. Löwen, "Swimming trajectories of a three-sphere microswimmer near a wall," *J. Chem. Phys.* **148**, 134904 (2018).
- ⁵⁰A. Daddi-Moussa-Ider, M. Lisicki, and A. J. T. M. Mathijssen, "Tuning the upstream swimming of microrobots by shape and cargo size," *Phys. Rev. Appl.* **14**, 024071 (2020).
- ⁵¹A. C. H. Tsang, P. W. Tong, S. Nallan, and O. S. Pak, "Self-learning how to swim at low Reynolds number," *Phys. Rev. Fluids* **5**, 074101 (2020).
- ⁵²B. Hartl, M. Hübl, G. Kahl, and A. Zöttl, "Microswimmers learning chemotaxis with genetic algorithms," *Proc. Natl. Acad. Sci. U. S. A.* **118**, e2019683118 (2021).
- ⁵³Z. Zou, Y. Liu, Y. N. Young, O. S. Pak, and A. C. H. Tsang, "Gait switching and targeted navigation of microswimmers via deep reinforcement learning," *Commun. Phys.* **5**, 158 (2022).
- ⁵⁴S. Paz, R. F. Ausas, J. P. Carbajal, and G. C. Buscaglia, "Chemoreception and chemotaxis of a three-sphere swimmer," *Commun. Nonlinear Sci. Numer. Simul.* **117**, 106909 (2023).
- ⁵⁵Y. Liu, Z. Zou, O. S. Pak, and A. C. H. Tsang, "Learning to cooperate for low-Reynolds-number swimming: A model problem for gait coordination," *Sci. Rep.* **13**, 9397 (2023).
- ⁵⁶D. F. Katz, "On the propulsion of micro-organisms near solid boundaries," *J. Fluid Mech.* **64**, 33–49 (1974).
- ⁵⁷L. J. Fauci and A. McDonald, "Sperm motility in the presence of boundaries," *Bull. Math. Biol.* **57**, 679–699 (1995).
- ⁵⁸J. P. Hernandez-Ortiz, C. G. Stoltz, and M. D. Graham, "Transport and collective dynamics in suspensions of confined swimming particles," *Phys. Rev. Lett.* **95**, 204501 (2005).
- ⁵⁹E. Lauga, W. R. DiLuzio, G. M. Whitesides, and H. A. Stone, "Swimming in circles: Motion of bacteria near solid boundaries," *Biophys. J.* **90**, 400–412 (2006).
- ⁶⁰D. J. Smith, E. A. Gaffney, J. R. Blake, and J. C. Kirkman-Brown, "Human sperm accumulation near surfaces: A simulation study," *J. Fluid Mech.* **621**, 289–320 (2009).
- ⁶¹D. Giacché, T. Ishikawa, and T. Yamaguchi, "Hydrodynamic entrapment of bacteria swimming near a solid surface," *Phys. Rev. E* **82**, 056309 (2010).
- ⁶²H. Shum, E. A. Gaffney, and D. J. Smith, "Modelling bacterial behaviour close to a no-slip plane boundary: The influence of bacterial geometry," *Proc. R. Soc. A* **466**, 1725–1748 (2010).
- ⁶³D. G. Crowdy and Y. Or, "Two-dimensional point singularity model of a low-Reynolds-number swimmer near a wall," *Phys. Rev. E* **81**, 036313 (2010).
- ⁶⁴A. Zöttl and H. Stark, "Nonlinear dynamics of a microswimmer in Poiseuille flow," *Phys. Rev. Lett.* **108**, 218104 (2012).
- ⁶⁵S. E. Spagnolie and E. Lauga, "Hydrodynamics of self-propulsion near a boundary: Predictions and accuracy of far-field approximations," *J. Fluid Mech.* **700**, 105–147 (2012).
- ⁶⁶G.-J. Li and A. M. Ardekani, "Hydrodynamic interaction of microswimmers near a wall," *Phys. Rev. E* **90**, 013010 (2014).
- ⁶⁷P. Bayati, M. N. Popescu, W. E. Uspsal, S. Dietrich, and A. Najafi, "Dynamics near planar walls for various model self-phoretic particles," *Soft Matter* **15**, 5644–5672 (2019).
- ⁶⁸A. Farutin, H. Wu, W. F. Hu, S. Rafaï, P. Peyla, M. C. Lai, and C. Misbah, "Analytical study for swimmers in a channel," *J. Fluid Mech.* **881**, 365–383 (2019).
- ⁶⁹B. U. Felderhof, "Swimming at low Reynolds number of a cylindrical body in a circular tube," *Phys. Fluids* **22**, 113604 (2010).
- ⁷⁰S. Jana, S. H. Um, and S. Jung, "Paramecium swimming in capillary tube," *Phys. Fluids* **24**, 041901 (2012).
- ⁷¹L. Zhu, E. Lauga, and L. Brandt, "Low-Reynolds-number swimming in a capillary tube," *J. Fluid Mech.* **726**, 285–311 (2013).

- ⁷²R. Ledesma-Aguilar and J. M. Yeomans, “Enhanced motility of a microswimmer in rigid and elastic confinement,” *Phys. Rev. Lett.* **111**, 138101 (2013).
- ⁷³B. Liu, K. S. Breuer, and T. R. Powers, “Propulsion by a helical flagellum in a capillary tube,” *Phys. Fluids* **26**, 011701 (2014).
- ⁷⁴H. O. Caldag and S. Yesilyurt, “Trajectories of magnetically-actuated helical swimmers in cylindrical channels at low Reynolds numbers,” *J. Fluids Struct.* **90**, 164–176 (2019).
- ⁷⁵Z. Ouyang, Z. Lin, Z. Yu, J. Lin, and N. Phan-Thien, “Hydrodynamics of an inertial squirmer and squirmer dumbbell in a tube,” *J. Fluid Mech.* **939**, A32 (2022).
- ⁷⁶R. Golestanian and A. Ajdari, “Analytic results for the three-sphere swimmer at low Reynolds number,” *Phys. Rev. E* **77**, 036308 (2008).
- ⁷⁷T. Bohlin, *On the drag on a rigid sphere moving in a viscous liquid inside a cylindrical tube*, Kungl. Tekniska Hogskolans handlingar (Elander, Molnlycke, Sweden, 1960).
- ⁷⁸A. Daddi-Moussa-Ider, M. Lisicki, and S. Gekle, “Hydrodynamic mobility of a sphere moving on the centerline of an elastic tube,” *Phys. Fluids* **29**, 111901 (2017).
- ⁷⁹A. Daddi Moussa Ider, “Diffusion of nanoparticles nearby elastic cell membranes: A theoretical study,” Ph.D. thesis (Universität Bayreuth, Germany, 2017).
- ⁸⁰B. Cui, H. Diamant, and B. Lin, “Screened hydrodynamic interaction in a narrow channel,” *Phys. Rev. Lett.* **89**, 188302 (2002).
- ⁸¹N. Liron and R. Shahar, “Stokes flow due to a Stokeslet in a pipe,” *J. Fluid Mech.* **86**, 727–744 (1978).
- ⁸²A. M. Leshansky, “Enhanced low-Reynolds-number propulsion in heterogeneous viscous environments,” *Phys. Rev. E* **80**, 051911 (2009).
- ⁸³H. C. Fu, V. B. Shenoy, and T. R. Powers, “Low-Reynolds-number swimming in gels,” *Europhys. Lett.* **91**, 24002 (2010).
- ⁸⁴N. Ho, S. D. Olson, and K. Leiderman, “Swimming speeds of filaments in viscous fluids with resistance,” *Phys. Rev. E* **93**, 043108 (2016).
- ⁸⁵K. Leiderman and S. D. Olson, “Swimming in a two-dimensional Brinkman fluid: Computational modeling and regularized solutions,” *Phys. Fluids* **28**, 021902 (2016).
- ⁸⁶A. Daddi-Moussa-Ider and A. M. Menzel, “Dynamics of a simple model microswimmer in an anisotropic fluid: Implications for alignment behavior and active transport in a nematic liquid crystal,” *Phys. Rev. Fluids* **3**, 094102 (2018).
- ⁸⁷A. Daddi-Moussa-Ider, Y. Hosaka, A. Vilfan, and R. Golestanian, “Axisymmetric monopole and dipole flow singularities in proximity of a stationary no-slip plate immersed in a Brinkman fluid,” *Phys. Rev. Res.* **5**, 033030 (2023).
- ⁸⁸Y. Hosaka, R. Golestanian, and A. Daddi-Moussa-Ider, “Hydrodynamics of an odd active surfer in a chiral fluid,” *New J. Phys.* (unpublished).
- ⁸⁹A. Daddi-Moussa-Ider, C. Kurzthaler, C. Hoell, A. Zöttl, M. Mirzakhloo, M.-R. Alam, A. M. Menzel, H. Löwen, and S. Gekle, “Frequency-dependent higher-order Stokes singularities near a planar elastic boundary: Implications for the hydrodynamics of an active microswimmer near an elastic interface,” *Phys. Rev. E* **100**, 032610 (2019).
- ⁹⁰S. Dalal, A. Farutin, and C. Misbah, “Amoeboid swimming in a compliant channel,” *Soft Matter* **16**, 1599–1613 (2020).